Taylor & Francis
Taylor & Francis Group

Shear and distensile fracture behaviour of Ti-based composites with ductile dendrites

Z. F. ZHANG*†‡, G. HE‡§ and J. ECKERT‡¶

†Shenyang National Laboratory for Materials Science, Institute of Metal Research, Chinese Academy of Sciences, Wenhua Road 72, 110016 Shenyang, PR China
‡Leibniz Institute for Solid State and Materials Research, Institute of Metallic Materials, P.O. Box 270016, D-01171 Dresden, Germany
§Light Materials Group, National Institute for Materials Science, 1-2-1 Sengen, Tsukuba, Ibaraki 305-0047, Japan
¶Department of Materials and Geosciences, Physical Metallurgy Division, Darmstadt University of Technology, Petersenstr. 23, D-64287 Darmstadt, Germany

The room-temperature deformation and fracture behaviour of Ti-based composites with ductile dendrites, prepared by copper mold casting and arc-melting techniques, was investigated. Under compressive loading, the Ti-based composites display high fracture strength (about 2000 MPa) and good ductility (about 4 or 10%). The yield strength of the Ti-based composites is relatively low (about 565–923 MPa). However, they have a large strain-hardening ability before failure, due to the interactions between shear bands and dendrites. For the arc-melted Ti-based composites, fracture often occurs in a shear mode with a high plasticity (about 10%). In contrast, the cast Ti-based composites break or split into several parts with a compressive plasticity of 4%, rather than failing in a shear mode. A new fracture mechanism, i.e. distensile fracture, is proposed for the first time to elucidate the failure of the as-cast Ti-based composites. Based on the difference in the fracture modes of the differently prepared composites, the relationships between shear and distensile fracture mechanisms and the corresponding fracture criteria are discussed.

Keywords: Ti-based composite; Dendrites; Shear fracture; Distensile fracture; Shear bands

1. Introduction

With the recent development of new alloys and suitable synthesis techniques, bulk metallic glasses (BMGs) or nano-structured composites can now be fabricated successfully, which allows for an in-depth investigation of their mechanical

*Corresponding author. Email: zhfzhang@imr.ac.cn

properties and their potential applications in many areas [1–6]. A large number of investigations show that BMGs and nano-structured materials mainly deform plastically by localized shear bands and, consequently, often display little plasticity before fracture at room temperature [7–11]. With the improvement of the fracture strength, the plasticity until failure is significantly decreased in almost all BMGs and nano-structural materials, which limits their application as structural materials.

Recently, several attempts were devoted to the synthesis of such composites either by introducing nano-crystals [5, 12–16], strong fibres [17–20], or ceramic particles [18, 21, 22]. However, the plasticity of the BMG composites containing nano-crystals or ceramic particles is not improved significantly, but sometimes the BMG composites even display a lower strength and zero plasticity due to the increase in the volume fraction of brittle nano-scale intermetallic compounds. Therefore, in order to further improve the plasticity, BMG or nano-structured composites with ductile dendritic phases were fabricated, respectively, for example, by Hays *et al.* [2], He *et al.* [3, 4] and Das *et al.* [1]. The first BMG composite containing a ductile dendritic phase was obtained in a Zr-based alloy, which displays a compressive plasticity of about 7% [2]. In comparison with Zr-based composites, Ti-based alloys have been much less investigated due to their poor glass-forming ability [23–25]. Recently, He *et al.* [3, 4, 26, 27] successfully fabricated different Ti-based BMG composites with ductile dendrites by the copper mold casting technique. The as-cast Ti-based composites possess both high strength (2400 MPa) and good ductility (14.5%), which is promising for the future development of advanced Ti-based composites. This paper reports on Ti-based composites containing dendrites, which were either synthesized by copper mold casting or by simple arc-melting. We first compare the differences in the mechanical properties of the Ti-based composites.

On the other hand, with the development of BMG composites, their mechanical properties and the corresponding deformation and fracture mechanisms have attracted widespread interest due to scientific curiosity as well as their possible technological applications. Spaepen [11] established an empirical deformation map and two typical deformation modes, i.e. homogenous and inhomogeneous flow respectively, at low temperature and high stress or high temperature and low stress. Inhomogeneous flow is typically concentrated in shear bands and the corresponding fracture always occurs in a shear mode, resulting in the formation of a vein-like structure on the fracture surface [10, 28–32]. A localized shear band is assumed to form by the build-up of free volume, created during the shearing of small groups of atoms [7, 11] or by the coalescence of the free volume upon cessation of plastic flow [9]. So far, all the constitutive equations associated with the plastic deformation of BMGs are based on shear localization [31, 33]. However, the newly developed BMG composites containing ceramic particles, strong fibres or ductile dendritic phases often exhibit multifarious fracture behaviour, and pure shear fracture sometimes does not take place [3, 4, 19, 20, 26, 27]. To date, the complex fracture phenomena in the new composites have never been considered and discussed in detail. Consequently, the second purpose of the present research is to elucidate the possible fracture phenomena in the Ti-based composites containing dendrites. Based on the present results, a new fracture mechanism, i.e. distensile fracture, is proposed to describe the fracture features in the composites.

2. Experimental procedure

For the present tests, two compositions, i.e. $Ti_{50}Cu_{23}Ni_{20}Sn_4Si_2B_1$ (TC1) and $Ti_{50}Cu_{22}Ni_{20}Sn_3Si_2B_3$ (TC2), were selected for the fabrication of Ti-based composites. First, Ti, Cu, Ni, Sn, Si and B with a purity of 99.9% were mixed and arc-melted to obtain master alloy ingots in a Ti-gettered argon atmosphere. Then, the master alloy ingots were re-melted several times to ensure homogeneity. One method for obtaining the composite samples was to cast the master alloy ingots into a copper mold of dimensions $\Phi\,3\,mm \times 100\,mm$ (or $\Phi\,5\,mm \times 100\,mm$). The other method was to prepare the composites (TM) by arc-melting the master alloy ingots several times and cooling at a slow rate.

   The two types of samples (TC and TM) were checked by standard X-ray diffraction (XRD) (Philips PW1050 diffractometer using Co Kα radiation) to identify the phase compositions. The microstructure of the samples was observed with a JEOL JSM-6400 scanning electron microscope (SEM). For the cast alloys (TC), the $\Phi\,3$ and $\Phi\,5\,mm$ rods were cut into $6\,mm$ and $10\,mm$ specimens for the compression tests. For the arc-melted alloy (TM), all the compression specimens were cut into dimensions of $3\,mm \times 3\,mm \times 6\,mm$. This specimen was carefully polished for observation of the surface deformation morphology. Compression tests were conducted at strain rates of 10^{-4} or 10^{-3}/s with an Instron 4652 testing machine at room temperature. After fracture, all specimens were investigated by SEM to reveal the surface deformation morphology and the fracture features.

3. Results

3.1. *Phase analysis and microstructure*

XRD analysis shows that the copper mold-cast Ti-based composites (TC1 and TC2) have the same diffraction pattern, independent of the diameter of the sample. For brevity, figure 1 only shows the XRD patterns of the $3\,mm$ diameter samples for the TC1 and TC2 alloys. There are two types of diffraction peaks, i.e. main peaks for a hcp Ti(Cu,Ni) solid solution and a second set of peaks for a Sn-rich phase with bcc structure. For the arc-melted samples (TM), the XRD pattern is relatively complicate and three types of phase can be observed, i.e. hcp Ti(Cu,Ni) and a Sn-rich phase as well as a Si-rich phase. This indicates that the fabrication process affects the phase formation in the Ti-based composites.

   SEM backscattering investigations were employed to resolve the microstructure of the two types of samples (TC and TM). As shown in figure 2, the microstructure mainly consists of three phases, i.e. a gray main phase with a dendritic-like structure, a white inter-dendritic matrix and a small amount of dark phase. The volume fractions of the three phases in the TM composite are similar to those in the TC composite (table 1). The volume fractions of the dark, white and gray phases in the composites are about 5, 35 and 60%, respectively. However, the dimension of the gray dendrites in the TM samples is clearly larger than that in the TC sample. This indicates that the cooling rate affects the microstructure of the samples and a slow cooling rate results in relatively coarse grains in the TM composite. Using EDX analysis, the compositions of the three phases were identified and the results are listed in table 1. The gray dendrites are a supersaturated hcp Ti(Ni,Cu) solid solution, which corresponds to the main XRD peak. The white inter-dendritic
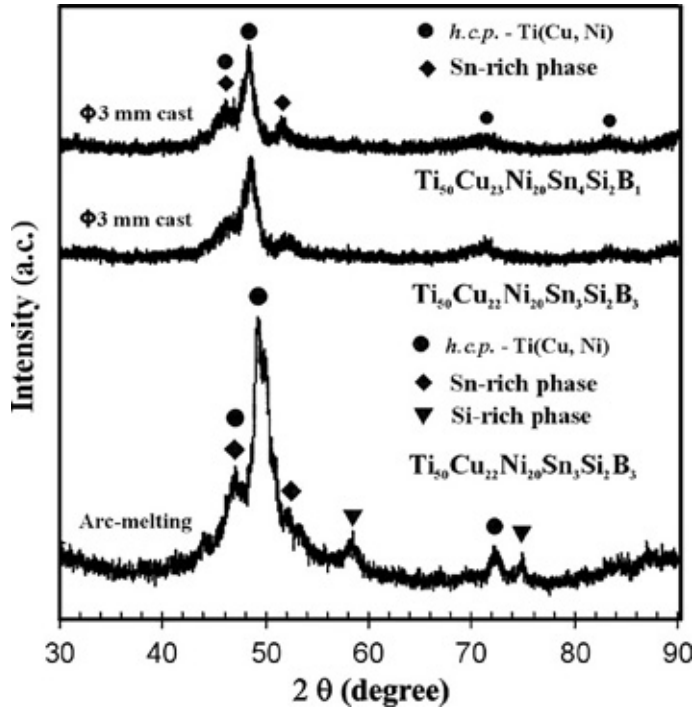
Figure 1. X-ray diffraction (XRD) patterns of the cast $Ti_{50}Cu_{23}Ni_{20}Sn_4Si_2B_1$ (TC1, Φ 3 mm) and $Ti_{50}Cu_{22}Ni_{20}Sn_3Si_2B_3$ (TC2, Φ 3 mm) composites and the arc-melted $Ti_{50}Cu_{22}Ni_{20}Sn_3Si_2B_3$ (TM).

phase is a Sn-rich Ti(Cu,Sn) solid solution and the black phase mainly contains a Si-rich (Ti,Cu) compound. This is consistent with the XRD patterns of figure 1. The present results are similar to the phases described for a $Ti_{50}Cu_{23}Ni_{20}Sn_7$ composite fabricated via the copper mold casting technique [26].

To clearly identify the dendritic phase in the Ti-based composites, some TM samples were cooled slowly after arc-melting. Then some free surfaces were observed by SEM without any polishing. In this case, the dendritic grains grew to a relatively large size and can be clearly seen, as shown in figure 3a. The dendritic grains are flower-like or snow-like and their branches nearly have the same size. The backscattered image in figure 3b shows the same morphology as in figure 3a.

3.2. *Compressive stress–strain curves*

Figure 4 shows the room-temperature compressive stress–strain curves of the Ti-based composites. The mechanical properties of all the samples are listed in table 2. From figure 4a, it can be seen that the yield strength of the cast samples (TC1 and TC2) is in the range of 762–923 MPa, and the final fracture strength reaches 1760–2050 MPa. This indicates that the cast Ti-based composites have a relatively low yield strength, but display a strong strain-hardening ability. Young's modulus of the composites is about 77.6–87.8 GPa, which is somewhat lower than that of Zr-based metallic glasses [15, 28, 29]. The plasticity at failure for all the cast samples (TC1 and TC2) is about 4.1–4.4%. Another feature is that both the yield
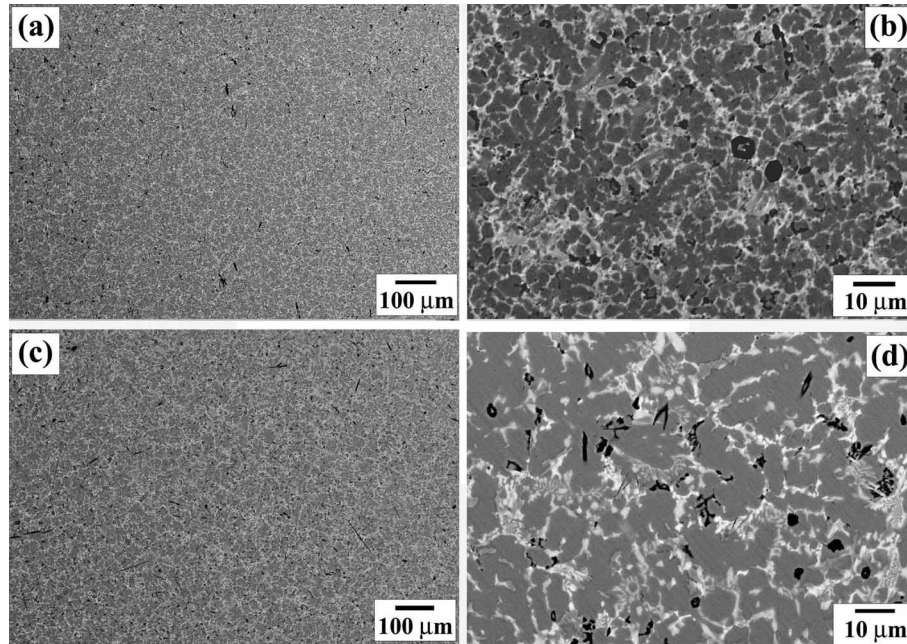
Figure 2. Microstructure of the $Ti_{50}Cu_{22}Ni_{20}Sn_3Si_2B_3$ alloy, subjected to copper mold casting (a, b) and prepared by arc-melting (c, d), observed by SEM and backscattering mode.

Table 1.   Compositions of the phases in the Ti-based composites.

	Ti (%)	Ni (%)	Cu (%)	Sn (%)	Si (%)	Volume fraction
White phase	65.86	8.43	10.15	14.69	0.87	$\approx 35\%$
Gray phase	49.90	28.84	19.17	0.97	1.13	$\approx 60\%$
Black phase	58.46	7.87	12.04	2.19	19.45	$\approx 5\%$
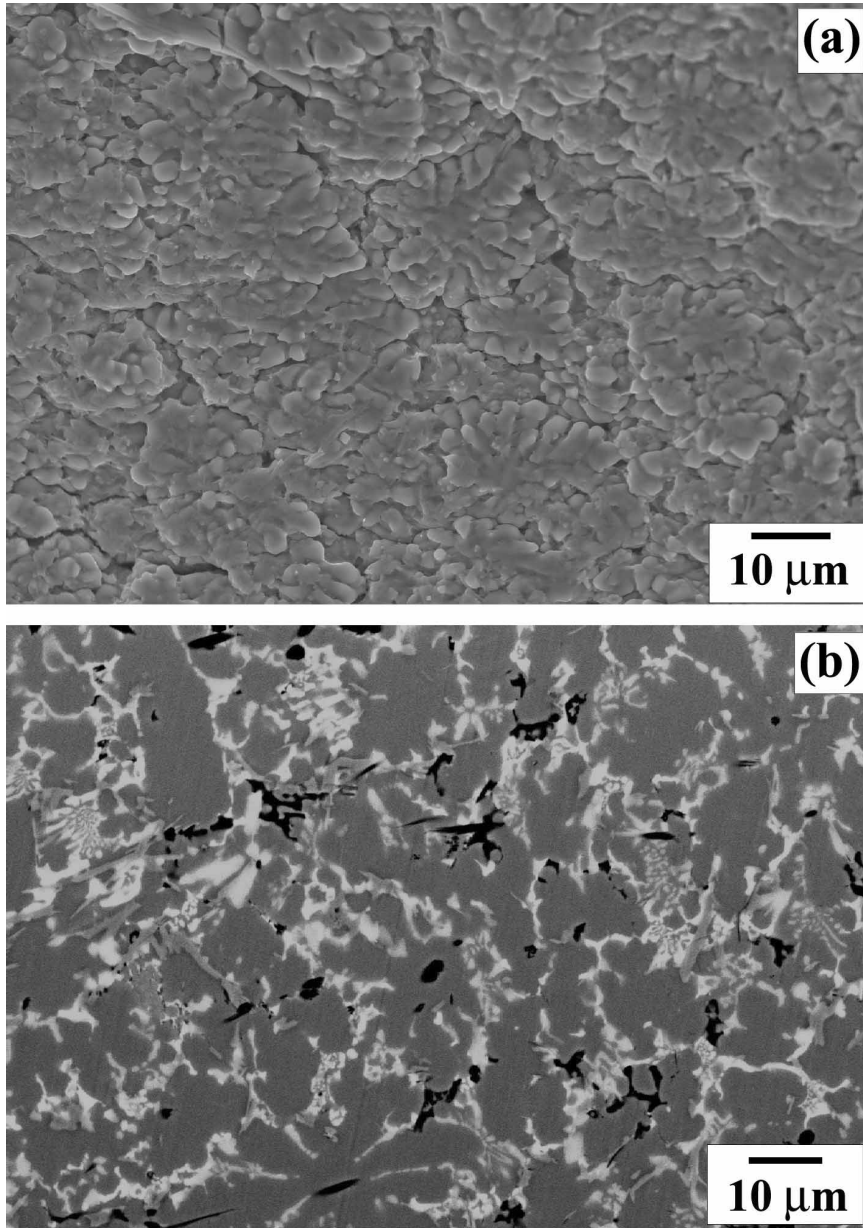
Figure 3.   Flower-like dendritic phase on the free surface of arc-melted $Ti_{50}Cu_{22}Ni_{20}Sn_3Si_2B_3$ (TM).
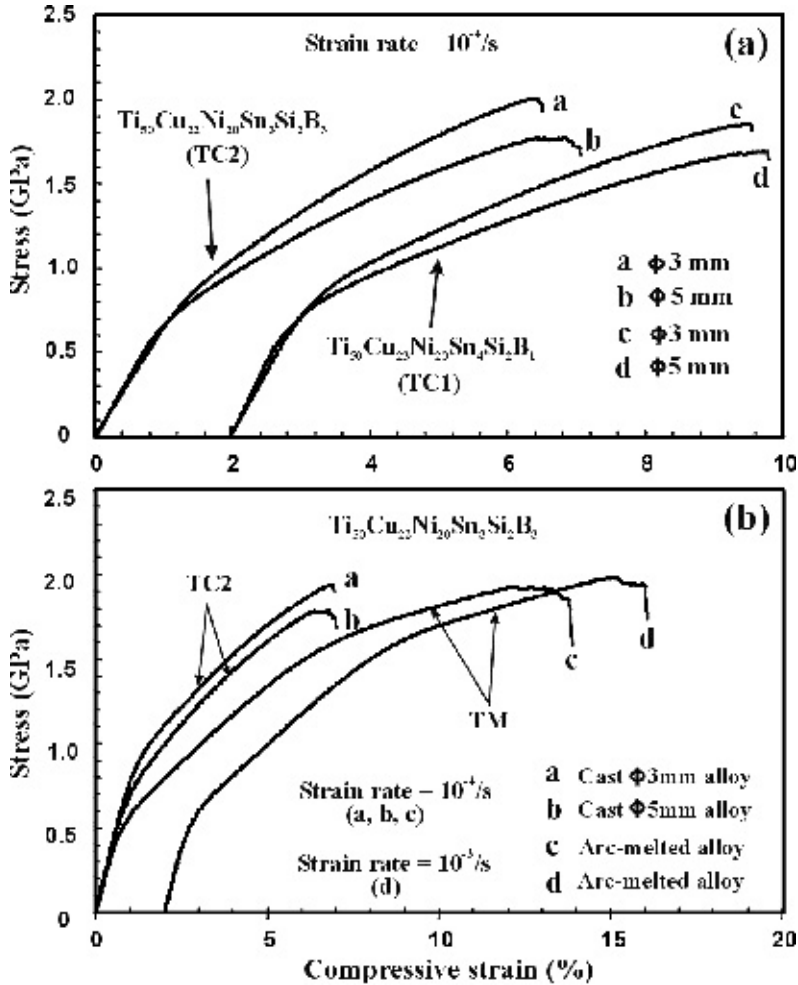
Figure 4. Compressive stress–strain curves of cast $Ti_{50}Cu_{23}Ni_{20}Sn_4Si_2B_1$ (TC1, Φ 3 mm and 5 mm) and $Ti_{50}Cu_{22}Ni_{20}Sn_3Si_2B_3$ (TC2, Φ 3 mm and 5 mm) composites and arc-melted $Ti_{50}Cu_{22}Ni_{20}Sn_3Si_2B_3$ (TM).

Table 2. Mechanical properties of the Ti-based composites with dendritic phases.

Composition	Sample size	Strain rate	σ_Y (MPa)	σ_F (MPa)	E (GPa)	ε_P (%)	ε_F (%)
$Ti_{50}Cu_{23}Ni_{20}Sn_4Si_2B_1$	$\Phi\,3 \times 6$ mm	10^{-4}/s	923	1940	84.1	4.28	7.42
(TC1)	$\Phi\,5 \times 10$ mm	10^{-4}/s	805	1760	87.8	4.36	7.61
$Ti_{50}Cu_{22}Ni_{20}Sn_3Si_2B_3$	$\Phi\,3 \times 6$ mm	10^{-4}/s	857	2050	77.6	4.07	6.45
(TC2)	$\Phi\,5 \times 10$ mm	10^{-4}/s	762	1790	80.4	4.14	6.67
$Ti_{50}Cu_{22}Ni_{20}Sn_3Si_2B_3$	$3 \times 3 \times 6$ mm^3	10^{-4}/s	565	1925	73.1	9.78	13.52
(TM)	$3 \times 3 \times 6$ mm^3	10^{-3}/s	586	1981	76.5	10.16	13.78

σ_Y, yield stress; σ_F, maximum fracture stress; E, Young's modulus; ε_P, ε_F, plastic strain and total strain at fracture.

and the fracture strength of the $\Phi 5\,$mm samples are lower than those of the $\Phi 3\,$mm samples. This implies that the diameter, or the cooling rate, also affects the yield and fracture strength of the composites, which was also observed for other Ti-based composites [3, 26, 27].

Figure 4b and table 2 clearly show that the yield strength of the Ti-based composites decreases in the order: cast $\Phi 3\,$mm, $\Phi 5\,$mm and the arc-melted sample. However, the plasticity of the arc-melted sample (TM) is improved to 9.8–10.2%, which is significantly higher than that (4.1–4.4%) of the cast samples (TC). On the other hand, the fracture strength (1925–1981 MPa) of the arc-melted samples (TM) is similar to that of the as-cast samples (TC). The fabrication conditions clearly change the plastic deformation capability of the Ti-based composites, and the arc-melted sample (TM) has a better plasticity than the cast samples (TC).

3.3. *Fractography and deformation morphology*

For fully amorphous alloys, failure always occurs in a shear mode due to the coalescence of shear bands [29–32]. However, for all the present cast samples (TC1 and TC2), failure does not take place in a pure shear mode, as shown in figure 5a. There are often several cracks in the samples and the samples finally break or split into several parts. This failure feature is clearly different from the shear fracture in fully amorphous alloys. However, a similar fracture mode was also observed in some BMG composites containing nano-crystals [14, 15], strong fibres [17–20] or a dendritic phase [3, 4, 27]. This indicates that the BMG composites often display multifarious fracture behaviour. Here, we define non-shear failure (break or split fracture) as distensile fracture and will discuss it in the following section.

Figures 5b and c show one of the fracture surfaces of the TC2 sample at different magnification. First, no sign of melting can be seen on the fracture surface. This indicates that the fracture mechanism of cast Ti-based alloys must be significantly different from that of fully amorphous alloys. Furthermore, it can be concluded that the melting phenomenon is not always associated with the fracture of BMG materials, and strongly depends on the details of the fracture mode. Large cracks can clearly be observed on most fracture surfaces of the cast samples, as indicated by the arrow in figure 5d. Large cracks are a typical casting defect occurring in copper mold casting. Furthermore, it is assumed that the large cracks should be correlated with distensile fracture of the cast composites.

Figure 6 shows the fracture feature of the arc-melted composites (TM), with failure clearly still occurring in a shear mode (see figure 6a) as for the fully amorphous alloys [8, 29, 31, 32]. The shear fracture surface makes an angle of about $32°$ with respect to the stress axis. This indicates that the shear fracture surface does not follow the maximum shear stress plane of the sample. Similar results were also obtained for other fully amorphous alloys and $Zr_{52.25}Cu_{28.5}Ni_{4.75}Al_{9.5}Ta_5$ composite containing Ta particles [22] (see table 3). The fracture surface of the arc-melted sample (TM) displays a relatively rough feature in comparison with the fully amorphous alloys. It is assumed that the rough fracture surfaces in the composites should be associated with strong interactions between shear bands and fibres, particles or dendrites, which result in a higher plasticity. The typical shear fracture feature is still a vein-like structure as observed at position A of the fracture surfaces in figure 6a. In the centre of the fracture surface (position B), there are many small cracks and melting is not observed, as shown in figure 6c. However, at the edge of the fracture
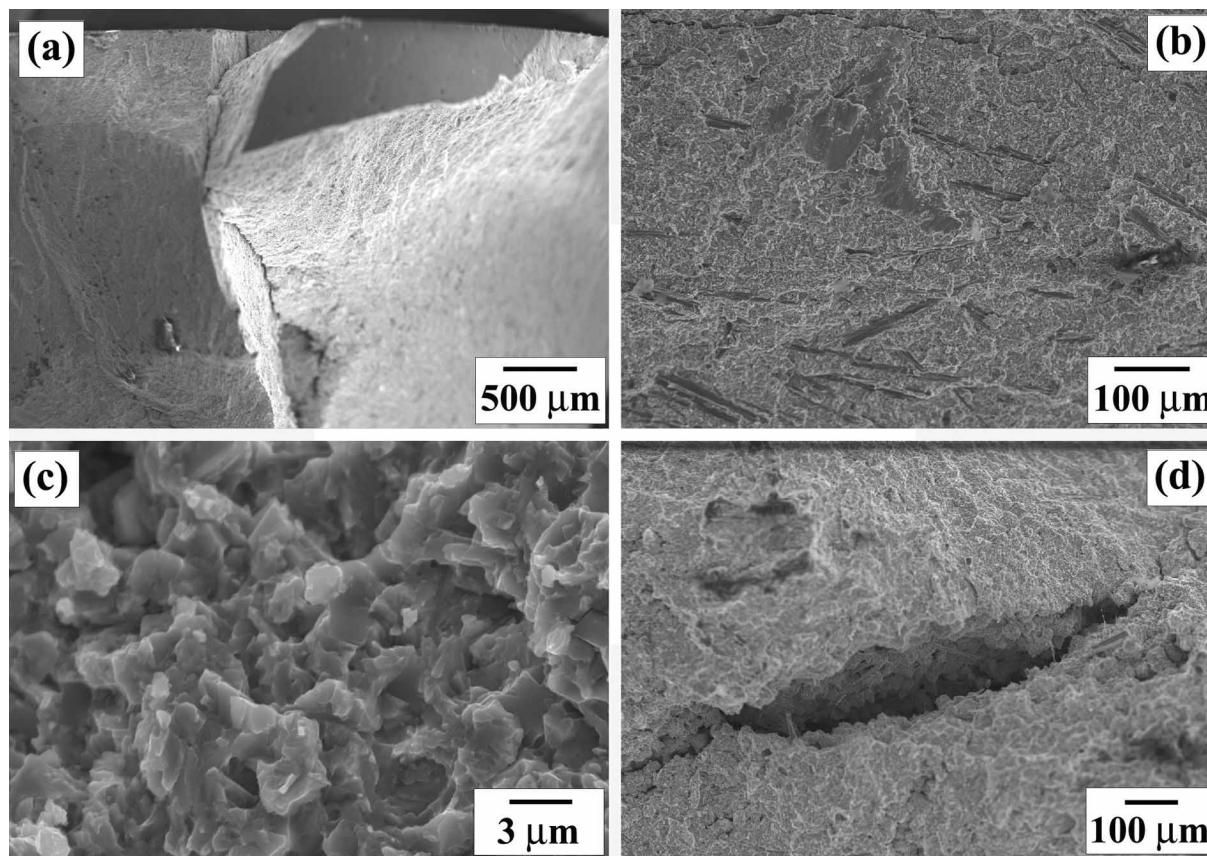
Figure 5. Compressive fracture surface features of the cast $Ti_{50}Cu_{22}Ni_{20}Sn_3Si_2B_3$ composite (TC2).
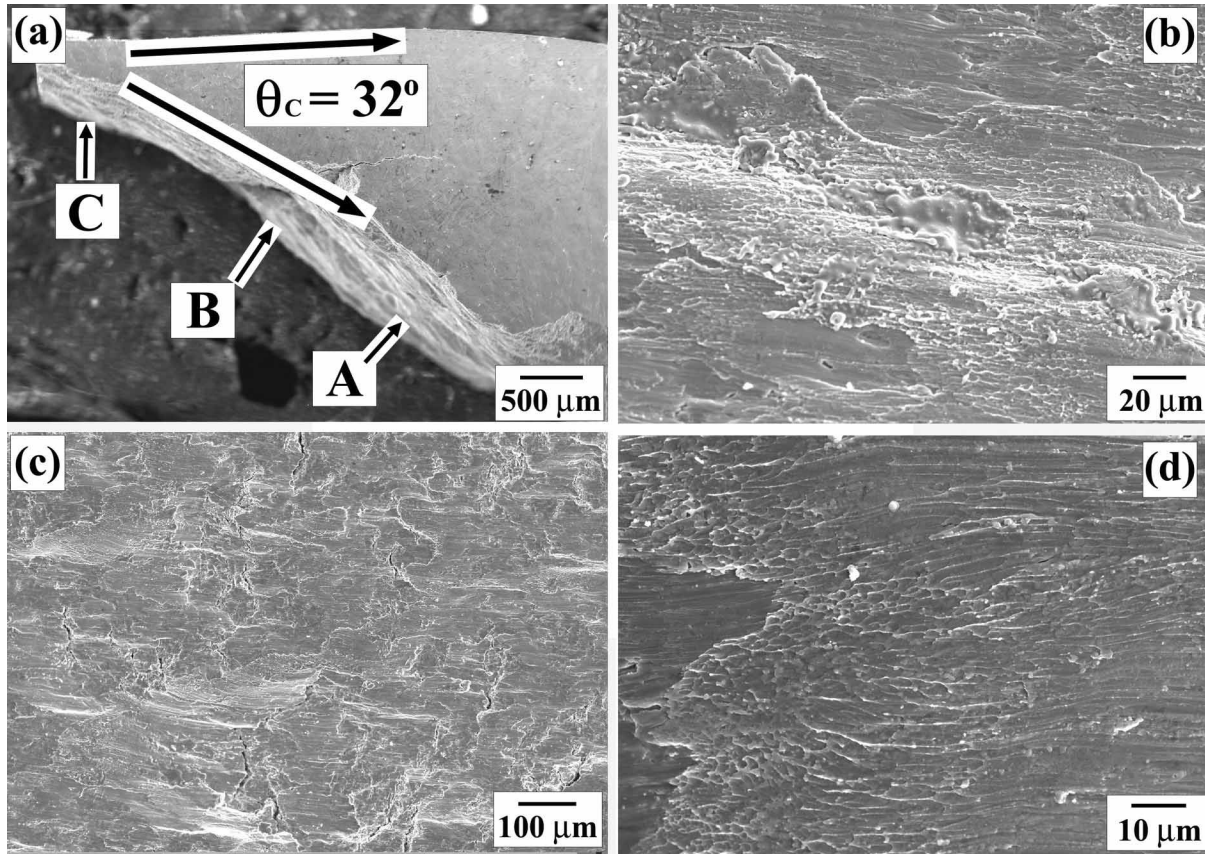
Figure 6.   Compressive fracture surface features of the arc-melted $Ti_{50}Cu_{22}Ni_{20}Sn_3Si_2B_3$ composite (TM).

Table 3. Comparison of the compressive fracture angle for different BMGs and composites.

Investigators	Composition	Microstructure	Fracture angle
Bian *et al.* [39]	$Zr_{55}Al_{10}Ni_5Cu_{30}$+CNT	BMG + nanocarbon tube	$\approx 41.3°$
Donovan [8]	$Pd_{40}Ni_{40}P_{20}$	Fully amorphous alloy	$41.9 \pm 1.2°$
He *et al.* [28]	$Zr_{52.5}Ni_{14.6}Al_{10}Cu_{17.9}Ti_5$	Fully amorphous alloy	40–45°
He *et al.* [22]	$(Zr_{0.55}Cu_{0.30}Al_{0.10}Ni_{0.05})_{1-95}Ta_5$	BMG + Ta particles	$\approx 32°$
Inoue *et al.* [40]	$Co_{43}Fe_{20}Ta_{5.5}B_{31.5}$	Fully amorphous alloy	$\approx 44°$
Inoue *et al.* [41]	$[(Fe_{0.8}Co_{0.2})_{0.75}B_{0.2}Si_{0.05}]_{96}Nb_4$	Fully amorphous alloy	$\approx 44°$
Lowhaphandu *et al.* [30]	$Zr_{62}Ti_{10}Ni_{10}Cu_{14.5}Be_{3.5}$	Fully amorphous alloy	$41.6 \pm 2.1°$
Wesseling *et al.* [42]	$Cu_{60}Zr_{20}Hf_{10}Ti_{10}$	Fully amorphous alloy	40.5°
Wright *et al.* [31]	$Zr_{40}Ti_{14}Ni_{10}Cu_{12}Be_{24}$	Fully amorphous alloy	$\approx 42°$
Xu *et al.* [36]	$Mg_{65}Cu_{7.5}Ni_{7.5}Zn_5Ag_5Y_{10}$+TiB$_2$	BMG+particles	40.2–42.4°
Zhang *et al.* [32]	$Zr_{59}Cu_{20}Al_{10}Ni_8Ti_3$	Fully amorphous alloy	$\approx 43°$
Zhang *et al.* [35]	$Zr_{52.5}Ni_{14.6}Al_{10}Cu_{17.9}Ti_5$	Fully amorphous alloy	$\approx 42°$
Present results	$Ti_{50}Cu_{22}Ni_{20}Sn_3Si_2B_3$ (TM)	Composite with dendrite	$\approx 32°$
	$Ti_{50}Cu_{23}Ni_{20}Sn_4Si_2B_1$ (TC1)	Composite with dendrite	Break or split
	$Ti_{50}Cu_{22}Ni_{20}Sn_3Si_2B_3$ (TC2)	Composite with dendrite	Break or split

surface (position C), melting induced by shear becomes more significant, as clearly shown in figure 6d. The above observations provide further evidence for the shear failure feature of the arc-melted samples (TM). The difference between figures 5 and 6 demonstrates that the fabrication conditions can affect the microstructure, which, in turn, determines the fracture mechanisms of the composites. The cast composites (TC) display a distensile fracture mode with a relatively low plasticity and no melting, but the arc-melted samples (TM) still fail in a shear mode with a relatively high plasticity and clear melting.

For a better understanding of the good ductility in the arc-melted composites (TM), sample surfaces were further investigated using the SEM backscattering technique. It can be seen from figure 7 that there are many shear bands over the whole surface of the TM samples. No obvious cracks can be observed at the interfaces between the dendrites and the matrix, indicating that these interfaces are sufficiently strong during compression. For the cast composites (TC) however, the shear bands are not well developed, which can be attributed to early distensile fracture during compression.

4. Discussion

Several classical theories or criteria have been proposed and developed in the past several hundred years concerning the fracture mechanisms of brittle materials (see, for example, Mayers and Chawla [34]). However, these fracture criteria mainly focus on brittle materials, such as ceramics, concrete, rock, etc. Investigation of the deformation and fracture mechanisms of BMG materials was rarely considered because BMG materials were only discovered and developed less than 20 years ago. It was found that the deformation of BMG materials always concentrated in shear bands which were approximately parallel to the maximum stress plane. However, recent observations have revealed that the fracture of fully amorphous alloys does not always proceed along the maximum shear stress plane, whether under tensile or compressive loading (table 3). This indicates that the Tresca criterion is invalid for the shear failure of BMG materials. This phenomenon has been explained by taking the effect of the normal stress into account [4, 8, 29, 31, 32, 35]. Therefore, for the present Ti-based composites containing dendrites, they fail either in a shear mode with angle $32°$, or in a distensile mode, depending on the detailed fabrication process. Therefore, the Mohr–Coulomb criterion can be considered for the shear fracture of various amorphous materials, i.e.

$$\tau_\theta - \mu\sigma_\theta \geq \tau_0. \tag{1}$$

Here, μ is a material constant, σ_θ and τ_θ are the normal and shear stress on any shear plane, and τ_0 is the critical shear fracture stress without normal stress. Furthermore, equation (1) can be plotted in $\sigma - \tau$ coordinates (figure 8a). The critical compressive fracture line is given by AB and the constant μ corresponds to the slope of the line. The specimen does not fracture if its stress state $(\sigma_\theta, \tau_\theta)$ on any plane is below the critical fracture line AB. The stress state $(\sigma_\theta, \tau_\theta)$ of a specimen can be described by the Mohr circle, and the diameter of the Mohr circle represents the applied compressive stress. With increasing applied load, the Mohr circle will become larger and finally contact the critical fracture line AB at contact point $\mathbf{C}(\sigma_\theta, \tau_\theta)$, which corresponds to the critical stress state at compressive shear fracture. Therefore,
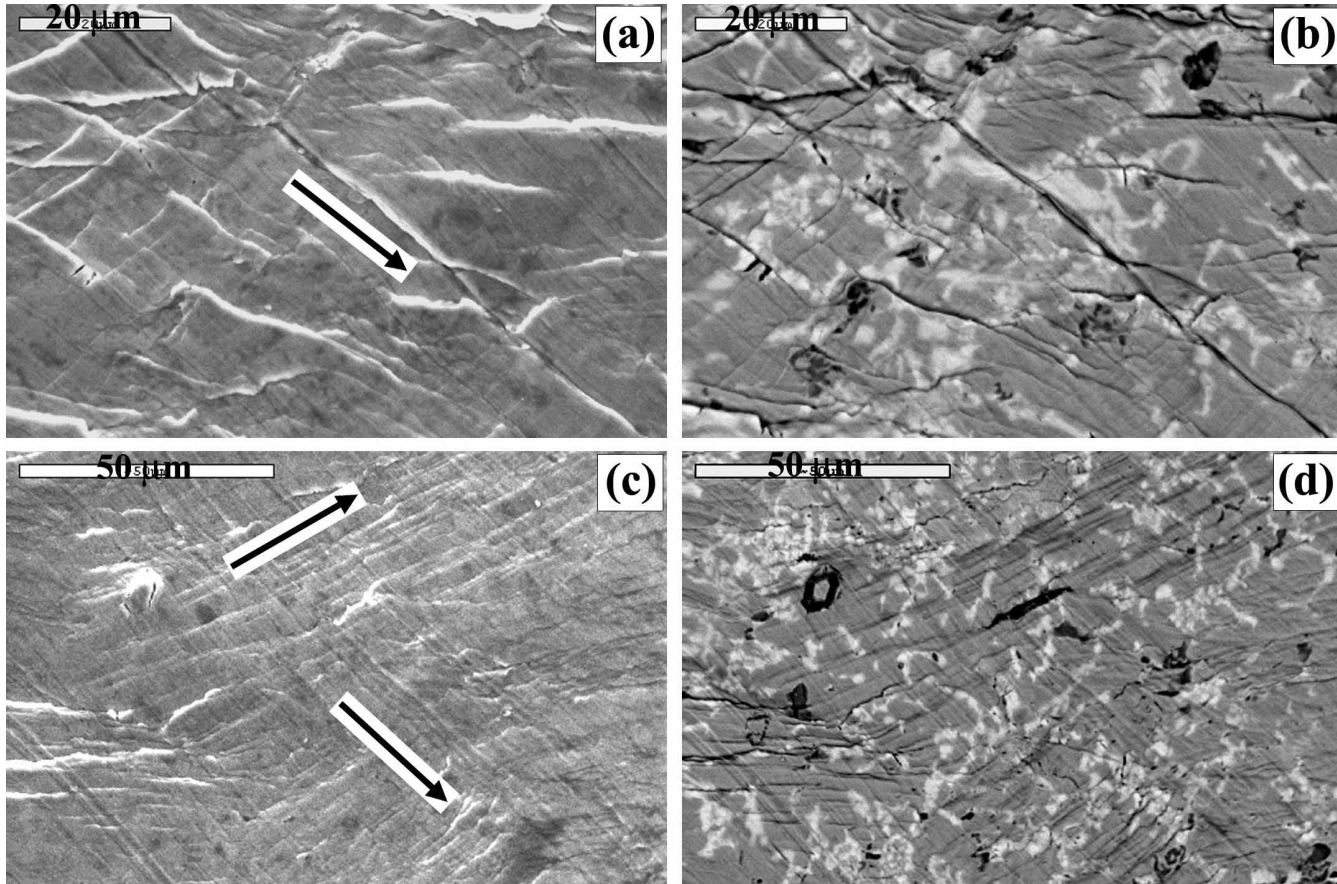
Figure 7. Interactions of the shear bands with the dendrites on the specimen surface of the arc-melted $Ti_{50}Cu_{22}Ni_{20}Sn_3Si_2B_3$ alloy (TM), observed by SEM and backscattering mode.
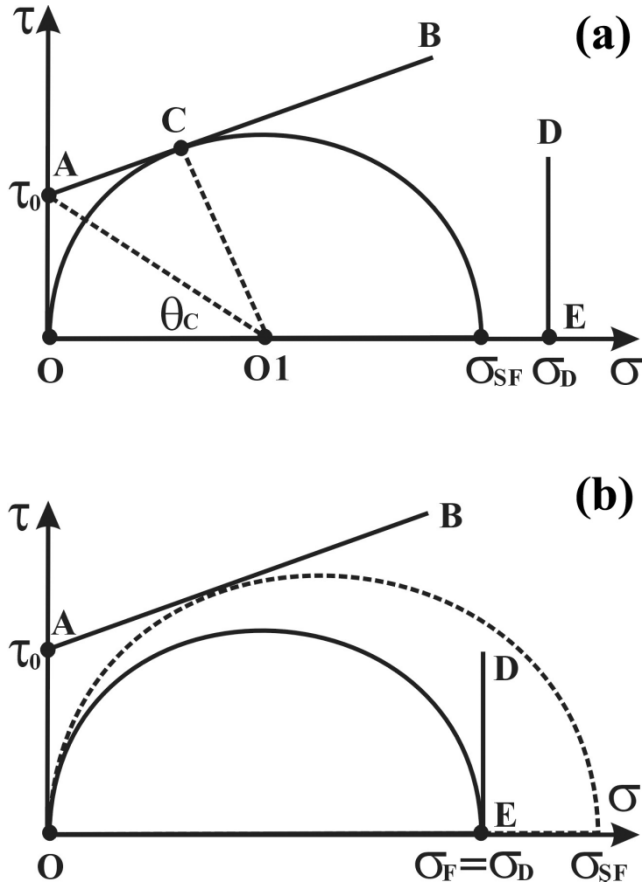
Figure 8. Schematic illustration of (a) the shear fracture and (b) the distensile fracture mechanism.

the diameter of the Mohr circle corresponds to the shear fracture strength σ_{SF} of the Ti-based composite and can be expressed as

$$\sigma_{SF} = \frac{2\tau_0}{\sqrt{1 + (\mu)^2} - \mu}. \tag{2}$$

Moreover, the angle of interaction between lines $\overline{OO1}$ and $\overline{O1C}$ is $2\theta_C$ and can be calculated as

$$\theta_C = \mathrm{arctg}\left(\sqrt{1 + (\mu)^2} - \mu\right) < 45°. \tag{3}$$

Therefore, it is easy to understand why θ_C is smaller than 45° for most amorphous alloys and some composites (table 3). Due to the strong effect of hard particles or ductile dendrites, Mg-, Zr- and Ti-based composites often fail at a relatively smaller fracture angle than fully amorphous alloys [8, 28–32, 36].

On the other hand, the introduction of ceramic particles or the precipitation of ductile dendrites in some composites may result in an inhomogeneous stress

distribution. As a result, macroscopic shear fracture does not occur in some composites containing ceramic particles, strong fibres or ductile dendrites. In the present work, all the cast Ti-based composites (TC) broke or were split into many parts, i.e. distensile fracture, compared with tensile fracture [35]. Here, we assume that there exists a distensile stress σ_D for some composites, as illustrated schematically in figure 8b. Accordingly, the critical distensile fracture line DE is shown in the figure. It is assumed that the final failure of a composite is the result of competition between shear fracture and distensile fracture, depending on the stress distribution throughout the whole specimen. When the distensile fracture stress σ_D is smaller than the critical shear fracture stress σ_{SF}, i.e.

$$\sigma_D < \sigma_{SF} = \frac{2\tau_0}{\sqrt{1 + (\mu)^2} - \mu}, \tag{4}$$

the stress Mohr circle will first contact the critical distensile fracture line DE prior to shear fracture, as shown in figure 8b. As a result, the specimen will first fail in a distensile mode rather than in a shear mode. This indicates that the specimen cannot bear much load before reaching its critical shear fracture strength σ_{SF} under compression.

For other brittle materials, such as polycrystalline ice [37], ceramics and rock [34], it is observed that their failure often occurs in a split or buckling mode under compression. It has been demonstrated that brittle glassy grain boundary phases often exist in ceramics due to the sintering agents that are added to the material to facilitate densification during processing [34]. Thus the brittle glassy grain boundary phases may fracture locally under shear resulting from compression. For a brittle material subjected to a compressive stress σ_C, Goodier [38] proposed a lateral tensile stress σ_T^L, which is related to σ_C by

$$\sigma_T^L = \frac{3(1 + 5\nu)}{2(7 - 5\nu)}\sigma_C = K\sigma_C, \tag{5}$$

where ν is the Poisson ratio of the material and K can be regarded as a material constant. It has been reported that the remote compressive stress σ_C can cause, by virtue of microstructural inhomogeneities, localized regions of tension, which, in turn, lead to crack initiation [34]. The microstructural inhomogeneities that can nucleate cracks mainly include voids, grain boundaries, glassy grain boundary phases, and second-phase particles, around which tensile stresses are generated by compression [34]. Therefore, the existence of lateral tensile stress σ_T^L is associated with the anisotropy of brittle materials and is a function of the compressive stress σ_C. Due to the presence of ductile dendrites in Ti-based composites, the stress distribution should be inhomogeneous and the degree of stress concentration will increase with increasing plastic strain. As can be seen in figure 5f, there are casting defects (or macro-cracks) within the TC samples. We believe that these macro-cracks are one of the reasons for the distensile fracture of the TC samples. When the stress concentration near the casting defects increases to a critical value, the TC sample cannot bear much load and will break or split rather than fracture in a shear mode.

From the above discussion, it can be concluded that the occurrence of distensile fracture, or shear fracture, strongly depends on the details of the microstructure of the composites. Ceramic particles, strong fibres or ductile

dendrites can further improve the critical fracture strength σ_F and the plasticity of the composites. This often results in a clear increase in the critical shear fracture stress τ_0 for these composites. Moreover, the constant μ of the composites is often increased due to the addition of reinforced phases to the composites. Accordingly, as shown in figures 8a and b, the critical conditions for shear and distensile fracture of the composites can be expressed by the relationship

$$\sigma_D > \sigma_{SF} \quad \text{(shear fracture)}, \tag{6a}$$

$$\sigma_D < \sigma_{SF} \quad \text{(distensile fracture)}. \tag{6b}$$

On the other hand, besides the applied stress and fracture strength of the composites, the effect of the strains in the composites cannot be omitted since their plasticity is relatively higher than that of monolithic glasses. As is well known, there is always a lateral tensile strain ε_L when a specimen is compressed to an axis strain ε_C, i.e.

$$\varepsilon_L = \nu \cdot \varepsilon_C. \tag{7}$$

If we consider the Poisson ratios ν of the TM and TC samples to be the same, the relationship between the axial compressive strain ε_C and the lateral tensile strain ε_L can be illustrated as in figure 9a. One can clearly see that the cast samples TC always have a lower compressive failure strain than the melting samples TM (see figure 4b). Normally, the failure of the cast samples TC occurs in a breaking (or distensile) mode, as shown in table 2 and illustrated in figure 9b. However, the melting samples TM fail in a shear fracture mode with an angle of $32°$ to the stress axis (see figures 6a and 9c). This indicates that distensile and shear fracture in the composites TC and TM are competing processes, depending on the detailed microstructure and the fabrication conditions. Here, as illustrated in figure 9a, we can define ε_C^C (6.5–7.6%) as the strain at compressive distensile fracture of the TC samples; ε_C^S (about 13.5%) is the strain at shear failure of the TM samples; ε_C^M is the possible
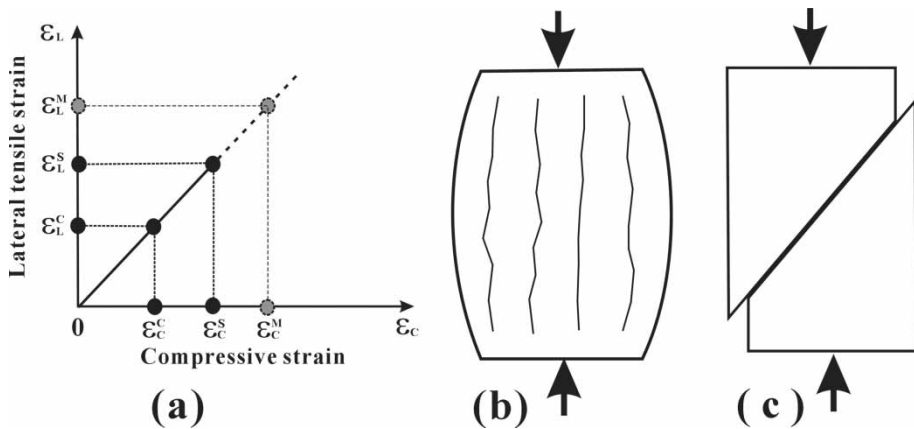

Figure 9. Schematic illustration of (a) compressive strain versus lateral tensile strain, (b) shear fracture, and (c) distensile fracture of the Ti-based composites.

strain at compressive distensile fracture of the TM samples (in the present samples, distensile fracture did not occur); ε_L^C, ε_L^S and ε_L^M are the lateral tensile strains caused by the compressive strains ε_C^C, ε_C^S and ε_C^M.

Since the cooling rate of the TC samples was significantly higher than that of the arc-melted TM samples, the cast samples TC must contain microstructures in a more unstable state, such as weak interfaces between the dendrites and matrix, and more defects and voids (see figure 5d). Thus, the microstructure of the TC sample requires a smaller lateral tensile strain for distensile fracture, finally resulting in easier distensile fracture under compression. However, the microstructure of the melting samples TM should be in a more equilibrium state, and contain strong interfaces between dendrites and the matrix, few defects and voids and more ductile dendrites. Therefore, they can carry more plastic strain than the TC samples, and do not exhibit a distensile fracture mode. Prior to distensile fracture, shear fracture becomes easier in the TM samples. Thus, as illustrated in figure 9a, the critical strains between the two failure modes in the TC and TM samples can simply be expressed as

$$\varepsilon_C^C < \varepsilon_C^S \quad \text{(shear fracture)}, \tag{7a}$$

$$\varepsilon_C^M > \varepsilon_C^S \quad \text{(distensile fracture)}. \tag{7b}$$

In summary, the occurrence of distensile fracture or shear fracture reflects the interactions of the reinforced phases with the matrix during deformation. Different fabrication conditions (or cooling rates) can result in a significant difference in the fracture modes and the failure strain even in the same alloys. Therefore, it is very important to understand the two fracture mechanisms, which will be beneficial for the fabrication and optimum design of newly developed composites containing suitable microstructures.

5. Conclusions

(1) Some Ti-based alloys can be fabricated to produce a composite containing a ductile dendritic phase either by copper mold casting or by using the arc-melting technique. $Ti_{50}Cu_{23}Ni_{20}Sn_4Si_2B_1$ (TC1) and $Ti_{50}Cu_{22}Ni_{20}Sn_3Si_2B_3$ (TC2) alloys prepared by copper mold casting yield a relatively low stress level of 762–932 MPa, but display a strong strain-hardening ability to fracture strength near 2000 MPa with a compressive plasticity of about 4%. Arc-melted $Ti_{50}Cu_{22}Ni_{20}Sn_3Si_2B_3$ (TM) alloy displays a higher compressive plasticity of about 10% and a fracture strength near 2000 MPa. It is suggested that arc-melting allows the fabrication of Ti-based composites with better ductility than copper mold casting.

(2) The Ti-based composites fail either in a shear mode or in a distensile mode under compression. It is assumed that the composite has two possible critical fracture stresses, i.e. shear fracture stress σ_{SF} and distensile fracture stress σ_D. Due to the presence of ductile dendrites, the critical shear fracture stress τ_0 and the constant μ of the composite is improved compared with fully amorphous alloys. The actual failure of a composite is a competitive process between shear and distensile fracture. The occurrence of distensile fracture

or shear fracture strongly depends on the detailed microstructure of the composite, or on the interactions between ductile dendrites and the matrix during deformation, which are very important for further optimization of composites with suitable microstructures.

Acknowledgements

References

[1] J. Das, W. Löser, U. Kühn, *et al.*, Appl. Phys. Lett. **82** 4690 (2003).
[2] C.C. Hays, C.P. Kim and W.L. Johnson, Phys. Rev. Lett. **84** 2901 (2000).
[3] G. He, J. Eckert, Q.L. Dai, *et al.*, Biomaterials **24** 5115 (2003).
[4] G. He, J. Eckert, W. Löser, *et al.*, Nature Mater. **2** 33 (2003).
[5] A. Inoue, T. Zhang, J. Saida, *et al.*, Mater. Trans. JIM **41** 1511 (2000).
[6] W.L. Johnson, MRS Bull. **24** 42 (1999).
[7] A.S. Argon, Acta metall. **27** 47 (1979).
[8] P.E. Donovan, Acta metall. **37** 445 (1989).
[9] R. Huang, Z. Suo, J.H. Prevost, *et al.*, J. Mech. Phys. Solids **50** 1011 (2002).
[10] C.A. Pampillo, J. Mater. Sci. **10** 1194 (1975).
[11] F. Spaepen, Acta metall. **25** 407 (1977).
[12] C. Fan, R.T. Ott and T.C. Hufnagel, Appl. Phys. Lett. **81** 1020 (2002).
[13] A. Inoue, T. Zhang and Y.H. Kim, Mater. Trans. JIM **38** 749 (1997).
[14] H. Kato, T. Hirano, A. Matsuo, *et al.*, Scripta mater. **43** 503 (2000).
[15] A. Leonhard, L.Q. Xing, M. Heilmaier, *et al.*, NanoStruct. Mater. **10** 805 (1998).
[16] L.Q. Xing, Y. Li, K.T. Ramesh, *et al.*, Phys. Rev. B **64** R180201 (2001).
[17] H. Choi-Yim, R. Busch, U. Köster, *et al.*, Acta mater. **47** 2455 (1999).
[18] H. Choi-Yim, R.D. Conner, F. Szuecs, *et al.*, Scripta mater. **45** 1039 (2001).
[19] R.D. Conner, R.B. Dandliker and W.L. Johnson, Acta mater. **46** 6089 (1998).
[20] R.D. Conner, H. Choi-Yim and W.L. Johnson, J. Mater. Res. **14** 3292 (1999).
[21] H. Choi-Yim, R.D. Conner, F. Szuecs, *et al.*, Acta mater. **50** 2737 (2002).
[22] G. He, Z.F. Zhang, W. Löser, *et al.*, Acta mater. **51** 2385 (2003).
[23] D.V. Louzguine and A. Inoue, Scripta mater. **43** 371 (2000).
[24] T. Zhang, A. Inoue and T. Masumoto, Mater. Sci. Engng. A **181/182** 1423 (1994).
[25] T. Zhang and A. Inoue, Mater. Trans. JIM **39** 1001 (1998).
[26] G. He, W. Löser, J. Eckert, *et al.*, J. Mater. Res. **17** 3015 (2002).
[27] G. He, W. Löser and J. Eckert, Acta mater. **51** 5223 (2003).
[28] G. He, J. Lu, Z. Bian, *et al.*, Mater. Trans. **42** 356 (2001).
[29] C.T. Liu, L. Heatherly and D.S. Easton, Metall. Mater. Trans. A **29** 1811 (1998).
[30] P. Lowhaphandu, L.A. Ludrosky, S.L. Montgomery, *et al.*, Intermetallics **8** 487 (2000).
[31] W.J. Wright, R. Saha and W.D. Nix, Mater. Trans. **42** 642 (2001).
[32] Z.F. Zhang, J. Eckert and L. Schultz, Acta mater. **51** 1167 (2003).
[33] J. Li, F. Spaepen and T.C. Hufnagel, Phil. Mag. A **82** 2633 (2002).
[34] M.A. Mayers and K.K. Chawla (Editors), *Mechanical Behavior of Materials* (Prentice Hall, Upper Saddle River, NJ, 1999).

[35] Z.F. Zhang, G. He, J. Eckert, *et al.*, Phys. Rev. Lett. **91** 04550501 (2003).

[36] Y.K. Xu, H. Ma, E. Ma, *et al.*, Acta mater. (submitted).

[37] I.J. Jordaan, Engng. Fract. Mech. **68** 1923 (2000).

[38] N. Goodier, J. appl. Mech. **1** 39 (1993).

[39] Z. Bian, T. Zhang, H. Kato, *et al.*, J. Mater. Res. **19** 1068 (2004).

[40] A. Inoue, B.L. Shen, H. Koshiba, *et al.*, Acta mater. **52** 1631 (2004).

[41] A. Inoue, B.L. Shen and C.T. Chang, Acta mater. **52** 4093 (2004).

[42] P. Wesseling, T.G. Nieh, W.H. Wang, *et al.*, Scripta mater. **51** 151 (2004).